PAPER

Design of nonlinear-Lamb-wave-based structural health monitoring systems with mitigated adhesive nonlinearity

IOP Publishing Smart Materials and Structures
Smart Mater. Struct. 27 (2018) 105006 (13pp) https://doi.org/10.1088/1361-665X/aad938

Design of nonlinear-Lamb-wave-based structural health monitoring systems with mitigated adhesive nonlinearity

Shengbo Shan[1,2], **Li Cheng**[1,2] and **Fuzhen Wen**[1,2]

[1] Department of mechanical engineering, The Hong Kong Polytechnic University, Kowloon, Hong Kong
[2] Hong Kong Branch of National Rail Transit Electrification and Automation Engineering Technology Research Center, The Hong Kong Polytechnic University, Hung Hom, Hong Kong

E-mail: li.cheng@polyu.edu.hk

Received 4 June 2018, revised 3 August 2018
Accepted for publication 9 August 2018
Published 4 September 2018

Abstract

Structural health monitoring (SHM) techniques with nonlinear Lamb waves offer the possibility of detecting incipient damages through the second harmonic generation. Particularly, the primary S0-secondary S0 Lamb wave mode pair in a weakly nonlinear plate is promising for SHM due to its appealing characteristics such as the cumulative second harmonic generation and flexible frequency selection. In a practical PZT-actuated SHM system, apart from the damage-related material nonlinearity of the plate (MNP), the adhesive nonlinearity (AN) is also proven to be a non-negligible nonlinear source, which may jeopardize damage diagnosis if not properly apprehended. By combining a nonlinear shear-lag model and the normal mode expansion method, a theoretical model is proposed in this work, which allows the investigation and the comparison of these two types of important nonlinearities in the system (AN and MNP). With the developed model, optimized nonlinear Lamb wave-based SHM systems can be designed with the mitigated influence of the undesired AN on the system. Finite element (FE) simulations are carried out to validate the proposed model and the effectiveness of the optimized systems through a tactical adjustment of the different nonlinear sources. The designed optimized system is verified by experiments, in comparison with an arbitrarily chosen one. The dominance level of the nonlinear sources in the two systems is evaluated through changing the MNP, which is realized by a thermal aging treatment. Both FE and experimental results demonstrate that the proposed model can effectively guide the design of SHM systems to mitigate AN so that the MNP can be well measured and further used as an indicator of the incipient structural damage.

Keywords: second harmonic Lamb waves, adhesive nonlinearity, material nonlinearity of plate, thermal aging

(Some figures may appear in colour only in the online journal)

Introduction

Structural health monitoring (SHM) techniques with Lamb waves have been a hot research topic for years since they provide the capability of enhancing the structural safety and reducing the maintenance cost in many industrial areas [1–3]. Classical Lamb-wave-based SHM methods usually rely on the scattering feature of the guided waves to characterize structural damage. The detection limit of these methods is dependent on the wavelengths of the Lamb waves in use, typically in the millimeter range in most cases [4–6]. For more relevant engineering applications, shifting the detection limit to the microstructural level to achieve an early damage detection can significantly facilitate the maintenance decisions. This hatches out the nonlinear-Lamb-wave-based SHM (NLW-SHM) techniques [7–9]. Specifically, techniques based on the nonlinear second harmonic Lamb waves are widely studied to characterize the microstructural changes

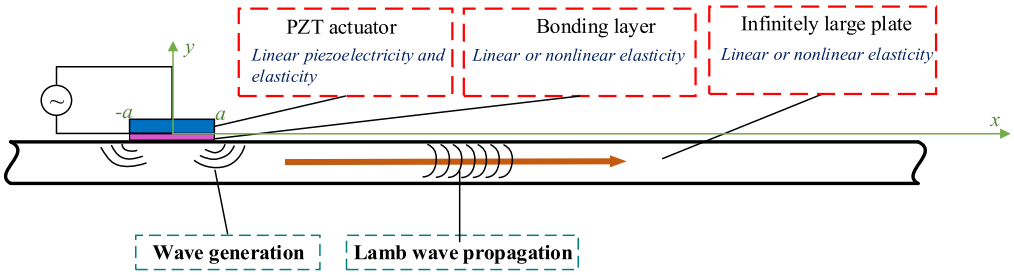

Figure 1. Sketch of the theoretical model.

during the processes of fatigue [10], plastic deformation [11] and thermal aging [9, 12] etc.

As the basis of the NLW-SHM techniques, a good understanding and control of the propagating characteristics of the second harmonic Lamb waves in a weakly nonlinear structure, typically a thin-walled plate, are crucial. Previous studies show that the second harmonic wave modes exist if only the power flux from the primary wave modes to the second harmonic wave modes is non-zero. In addition, if the phase velocities of the primary waves and the second harmonic waves match, the amplitude of the second harmonic waves will be cumulative with respect to the propagating distance. Otherwise, it will bound [13–16]. The cumulative feature facilitates the SHM in two aspects. First, the amplitude of the cumulative second harmonic Lamb waves increases with the propagating distance, thus facilitating their acquisition. Second, as the cumulative feature is uniquely associated with the distributed material nonlinearity of the plate (MNP), the slope of the cumulation curve can be used as a damage indicator for SHM [17]. However, due to the dispersive characteristics of the Lamb waves, only a limited number of mode pairs in the relatively high-frequency range can strictly satisfy both conditions for the cumulative second harmonic generation [15]. This leaves very limited options for the excitation frequency selection, which hampers the NLW-SHM applications to a certain extent.

Recently, it is reported that the primary S0- secondary S0 Lamb wave mode pair can approximately satisfy the phase matching condition due to their slightly dispersive characteristics in the relatively low-frequency range. Thus, the second harmonic S0 mode Lamb waves can be quasi-cumulative [18]. The choice of the excitation frequencies to generate this specific mode pair then becomes very flexible. This offers great convenience for SHM applications like the evaluation of microstructural changes. For example, Wan *et al* [19] used the low-frequency S0 mode pair to characterize local microscale damage numerically through the reflected and transmitted second harmonic generation. Sun *et al* [20] studied the case of plasticity-driven damage in the numerical perspective. All these efforts demonstrate the promises of using the second harmonic S0 mode Lamb waves to monitor microstructural changes.

To build a self-contained NLW-SHM system, transducers are usually required to be permanently bonded on the host structure to realize the online and real-time monitoring. Piezoelectric wafer transducer (PZT) is the most popular option [21]. In a typical PZT-driven NLW-SHM system, apart from the MNP, which is supposed to be specific to damages, there exist other nonlinear sources which are non-negligible or can even overwhelm the effect of the MNP. If not properly apprehended, these nonlinear sources are detrimental and may jeopardize the diagnosis results. Specifically, the material nonlinearity of the bonding layer between the PZT transducer and the structure under inspection, which is referred as adhesive nonlinearity (AN), is proven to be non-negligible in a typical SHM system in our previous work [22, 23]. To realize a reliable damage diagnosis, the influence of the AN in a typical NLW-SHM system needs to be mitigated through proper system design. To achieve this, the influence of both the AN and MNP on the system should be thoroughly understood. This requires a comprehensive model which is capable of considering both the AN and the MNP under the same roof.

Motivated by this, this paper proposes a theoretical model by combining the previously developed nonlinear shear-lag solutions and the normal mode expansion (NME) method to investigate the frequency tuning characteristics of both AN-induced and MNP-induced Lamb waves in a PZT-driven NLW-SHM system. Guided by the theoretical model, a system design is carried out to mitigate the undesired AN through tuning the PZT dimensions. Two systems with mitigated AN are highlighted and compared to the one with an arbitrary PZT setting which exhibits dominant AN. Finite element (FE) models are developed to validate both the proposed model and the designed systems. Finally, experiments are carried out on samples through thermal aging treatment. The dominance level of the AN and MNP is assessed in both systems by tracking the changes of their second harmonic responses before and after the thermal aging process.

Theoretic basis

The theoretical model considers the 1D plane wave propagation in an infinitely large plate, as sketched in figure 1. A PZT transducer with finite width is bonded on the plate through an adhesive layer. In this model, the PZT is assumed to be linear in both elasticity and piezoelectricity while the bonding layer and the plate have nonlinear elastic properties. Previous studies [22] show that the effect of the AN in the actuating part is more significant than that in the sensing part. Therefore, only the PZT actuator is considered in this work.

To facilitate the model development, the NME framework is first introduced [24]. Under this framework, the solutions for

the linear and AN-induced Lamb waves are provided by integrating the previously calculated nonlinear shear-lag solutions. Finally, solutions for the MNP-induced responses are obtained.

NME method for Lamb wave generation

Consider two sources $\mathbf{F_1}$ and $\widetilde{\mathbf{F_2}}$ which generate two wave fields characterized by the velocity $\mathbf{v_1}$, $\widetilde{\mathbf{v}}_\mathbf{2}$ and stress $\mathbf{T_1}$, $\widetilde{\mathbf{T}}_\mathbf{2}$. Subscripts 1 and 2 denote the two systems while the overtilde represents the complex conjugate. The complex reciprocity theory [24] states:

$$\nabla(\widetilde{\mathbf{v}}_\mathbf{2}\cdot\mathbf{T_1}+\mathbf{v_1}\cdot\widetilde{\mathbf{T}}_\mathbf{2})=-(\widetilde{\mathbf{v}}_\mathbf{2}\cdot\mathbf{F_1}+\mathbf{v_1}\cdot\widetilde{\mathbf{F}}_\mathbf{2}). \tag{1}$$

For the Lamb wave generation problems, assume the solution to system 1 is the wave field by the source and expressed by the modal expansion as

$$\begin{aligned}\mathbf{v_1}(x,y)&=\sum_m a_m(x)\mathbf{v_m}(y),\\ \mathbf{T_1}(x,y)&=\sum_m a_m(x)\mathbf{T_m}(y),\end{aligned} \tag{2a}$$

where $\mathbf{v_m}(y)$ and $\mathbf{T_m}(y)$ are the velocity and stress corresponding to the wave structure (thickness-across distribution) of the mth Lamb wave modes, respectively, with details given in appendix. $a_m(x)$ is the modal participation factor. In the equation derivations, the time-harmonic term $e^{-i\omega t}$ is omitted for brevity. The solution to system 2 is assumed to be homogenous ($\mathbf{F}_2=0$), thus represented by a single Lamb wave mode as

$$\begin{aligned}\mathbf{v_2}(x,y)&=\mathbf{v_n}(y)e^{i\xi_n x}\\ \mathbf{T_2}(x,y)&=\mathbf{T_n}(y)e^{i\xi_n x}.\end{aligned} \tag{2b}$$

Putting the solutions (2*a*) and (2*b*) to the complex reciprocity equation (1) and rearranging with the modal orthogonal relation [24] yield:

$$\begin{aligned}4P_{nn}\left(\frac{\partial}{\partial x}-i\widetilde{\xi}_n\right)a_n(x)&=(\widetilde{\mathbf{v}}_\mathbf{n}\cdot\mathbf{T_1}+\mathbf{v_1}\cdot\widetilde{\mathbf{T}}_\mathbf{n})\cdot\hat{\mathbf{y}}\big|_{-d}^{d}\\&+\int_{-d}^{d}\widetilde{\mathbf{v}}_\mathbf{n}\cdot\mathbf{F_1}\mathrm{d}y\end{aligned} \tag{3a}$$

with

$$P_{nn}=\frac{1}{4}\int_{-d}^{d}[\widetilde{\mathbf{v}_\mathbf{n}(y)}\cdot\mathbf{T_n}(y)+\mathbf{v_n}(y)\cdot\widetilde{\mathbf{T}_\mathbf{n}(y)}]\cdot\hat{\mathbf{x}}\mathrm{d}y. \tag{3b}$$

The first term on the right-hand side of equation (3*a*) is the forcing function due to the surface traction and external velocity excitation while the second term is related to the volume force.

Linear and AN-induced Lamb wave responses with PZT excitations

In our previous work [22], the linear and AN-induced Lamb responses were calculated with the Fourier transform method once obtaining the linear and AN-induced shear stress distributions on the top of the plate. However, the Fourier transform method cannot provide the information on the mode participation factor for the further calculations of the MNP-induced responses. Therefore, the linear and AN-induced Lamb wave responses are revamped under the framework of the NME method.

For the linear and AN-induced wave generation problem, the main external excitation for the plate is the shear stress across the PZT-plate interface. Thus, the governing equation (3) retreats to:

$$4P_{nn}\left(\frac{\partial}{\partial x}-i\widetilde{\xi}_n\right)a_n(x)=\widetilde{\mathbf{v}_\mathbf{n}(d)}\cdot\boldsymbol{\tau}(x). \tag{4}$$

The shear stresses, responsible for the excitation of the linear and the AN-induced wave generation can be found in [22], as:

$$\tau_L(x)=\frac{G_{ba}\epsilon_{\mathrm{ISA}}}{t_{ba}\Gamma_a}\frac{\sinh(\Gamma x)}{\cosh(\Gamma a)}, \tag{5}$$

$$\begin{aligned}\tau_{AN}(x)=&-\left(\frac{2R}{3\Gamma^2}+P\right)\frac{\cosh(2\Gamma a)}{\cosh(\Gamma a)}\sinh(\Gamma x)\\&+\frac{R}{3\Gamma^2}\sinh(2\Gamma x).\end{aligned} \tag{6}$$

Various intermediate terms are expressed as:

$$\psi=\frac{t_h E_h}{t_a E_a}, \tag{7a}$$

$$\Gamma^2=\frac{G_{ba}}{t_{ba}t_a E_a}\frac{\alpha+\psi}{\psi}, \tag{7b}$$

$$P=\frac{(2B_{ba}+A_{ba})\varepsilon_{\mathrm{ISA}}{}^2}{4t_{ba}\Gamma(\cosh(\Gamma a))^2}, \tag{7c}$$

$$R=P\left(\frac{G_{ba}}{E_a t_a t_{ba}}-2\Gamma^2\right), \tag{7d}$$

$$\varepsilon_{\mathrm{ISA}}=\frac{d_{31a}V_{\mathrm{in}}}{t_a}. \tag{7e}$$

In the above equations, subscripts h, a and ba denote the host structure, actuator and bonding layer respectively. E and G are the Young's modulus and shear modulus of the elements respectively. t denotes the thickness and a is the half-width of the PZT patch. d_{31} is the piezoelectric constant and V_{in} the input voltage. A_{ba} and B_{ba} are the third-order elastic constants (TOECs) of the adhesive.

The solution to equation (4) can be further expressed as

$$a_n(x)=\frac{\widetilde{\mathbf{v}_\mathbf{n}(d)}}{4P_{nn}}\cdot e^{i\widetilde{\xi}_n x}\int_{-a}^{a}e^{-i\widetilde{\xi}_n\overline{x}}\boldsymbol{\tau}(\overline{x})\mathrm{d}\overline{x}. \tag{8}$$

Substituting either the linear or the AN-induced shear stress distribution (equations (5) or (6)) into (8), the corresponding modal participation factor can be obtained, resulting in the solution to the Lamb wave fields.

MNP-induced Lamb wave responses with PZT excitations

When Lamb waves propagate in the nonlinear elastic plate, the second harmonic responses due to the MNP will be generated. According to the Landau–Lifshitz model, the nonlinear stress–strain relation can be expressed as [15]:

$$\begin{aligned}\mathbf{T}=&\lambda\mathrm{tr}[\mathbf{E}]+2\mu\mathbf{E}+C(\mathrm{tr}[\mathbf{E}])^2\mathbf{I}+B\mathrm{tr}[\mathbf{E}^2]\mathbf{I}+2B\mathrm{tr}[\mathbf{E}]\mathbf{E}\\&+A\mathbf{E}^2,\end{aligned} \tag{9}$$

Table 1. Parameters used in the theoretical and FE models.

PZT 5					
Width	Thickness	E	v	d_{31}	e_{33}^{σ}
8–40 mm	0.3 mm	62 GPa	0.32	−210 pm V^{-1}	18.9 nF m^{-1}
Bonding layer[a]					
Thickness	E	v	A	B	C
0.03 mm	1.31 GPa	0.4	−20.9 GPa	−8.3 GPa	−6.1 GPa
Aluminum plate[b]					
Thickness	E	v	A	B	C
2 mm	69.56 GPa	0.34	−351.2 GPa	−149.4 GPa	−102.8 GPa

[a] The material parameters of the bonding layer can be referred to [22].
[b] The TOECs of the aluminum are referred to [25].

where λ and μ are Lamé constants, while A, B, C are defined as the TOECs of the plate. The operation tr() denotes the trace of a matrix. $\mathbf{T}$ is the second Piola–Kirchhoff stress tensor and $\mathbf{E}$ the Lagrangian strain tensor. The geometric nonlinearity is omitted as it is shown to be negligible in the present case. Then, the Lagrangian strains retreat to the engineering strains ε and the nominal stresses $\boldsymbol{\sigma}$ are used instead of the second Piola–Kirchhoff stresses in the following analyses.

Based on the perturbation theory, the stresses can be expressed with the linear part and nonlinear part, as

$$\begin{aligned}&\boldsymbol{\sigma} = \boldsymbol{\sigma}^{\mathbf{L}} + \boldsymbol{\sigma}^{\mathbf{NL}} \quad \text{with}\\ &\boldsymbol{\sigma}^{\mathbf{L}} = \lambda \mathrm{tr}[\varepsilon] + 2\mu\varepsilon, \quad \boldsymbol{\sigma}^{\mathbf{NL}} = C(\mathrm{tr}[\varepsilon])^2\mathbf{I} + B\mathrm{tr}[\varepsilon^2]\mathbf{I}\\ &\quad + 2B\mathrm{tr}[\varepsilon]\varepsilon + A\varepsilon^2.\end{aligned} \tag{10}$$

It is worth noting that the nonlinear part is calculated with the linear strains of the Lamb wave field obtained in the previous section. Then, the nonlinear surface traction $\mathbf{S}$ and the body force $\mathbf{f}$ which correspond to the second harmonic generation can be calculated as [15]

$$\mathbf{S} = -\boldsymbol{\sigma}^{\mathbf{NL}} \cdot \hat{\mathbf{y}}, \tag{11a}$$

$$\mathbf{f} = \nabla \cdot \boldsymbol{\sigma}^{\mathbf{NL}}. \tag{11b}$$

Using equation (11) in (3) gives:

$$\begin{aligned}4P_{nn}\left(\frac{\partial}{\partial x} - i\widetilde{\xi}_n\right)a_n(x) = \Bigg(&-\widetilde{\mathbf{v}}_{\mathbf{n}} \cdot \boldsymbol{\sigma}^{\mathbf{NL}} \cdot \hat{\mathbf{y}}|_{-d}^{d}\\ &+ \int_{-d}^{d} \widetilde{\mathbf{v}}_{\mathbf{n}} \cdot \nabla \cdot \boldsymbol{\sigma}^{\mathbf{NL}} \mathrm{d}y\Bigg)e^{i2kx} = f_n e^{i2kx},\end{aligned} \tag{12}$$

where k is the wave number of the primary wave field. The solution to equation (12) can be further obtained as:

$$a_n(x) = \frac{f_n}{4P_{nn}}\begin{cases}\dfrac{i}{\widetilde{\xi}_n - 2k}(e^{i2kx} - e^{i\widetilde{\xi}_n x}) & \text{for } \widetilde{\xi}_n \neq 2k\\ xe^{i2kx} & \text{for } \widetilde{\xi}_n = 2k.\end{cases} \tag{13}$$

According to equation (13), when the phase velocities of the fundamental and second harmonic Lamb waves match, the amplitude of the second harmonic Lamb waves is cumulative. Otherwise, it will bound with respect to the propagating distance. With the proposed method, the modal participation factors at different frequencies can be further calculated, resulting in the frequency tuning curves of the MNP-induced Lamb waves.

To sum up, in the proposed theoretical model, the frequency tuning curves of the AN-induced and MNP-induced Lamb waves generated by PZT actuators can be obtained, which allows the direct comparison between the influences of these two nonlinear sources in the SHM system. This will provide useful guidance for further system design.

Numerical studies

In this section, numerical studies are carried out with a two-fold purpose: to validate the proposed model on one hand and to ascertain the designed optimal NLW-SHM systems with mitigated AN on the other hand. First, the frequency tuning curves of the linear and AN-induced Lamb waves obtained using the current model with the NME method are cross-checked with those obtained from the Fourier transform method [22]. Then, the frequency tuning characteristics of the MNP-induced responses are validated with the FE simulations. The dependence of the frequency tuning characteristics on the wave propagating distances are investigated, providing physical insights on the frequency tuning phenomenon. After that, system design is carried out by evaluating three typical NLW-SHM systems with different widths of the PZT actuators. Through comparing their AN-induced and MNP-induced responses, the feasibilities of the systems for SHM are discussed. Finally, the influence of the primary A0- secondary S0 mode pair on the NLW-SHM systems is briefly analyzed.

The material parameters of the PZT, bonding layer and aluminum plate used in the simulations are tabulated in table 1. The voltage applied on the PZT actuator is set to 200 V.

Lamb wave tuning with FT and NME method

The frequency tuning characteristics of the linear and AN-induced responses, which were calculated with the Fourier

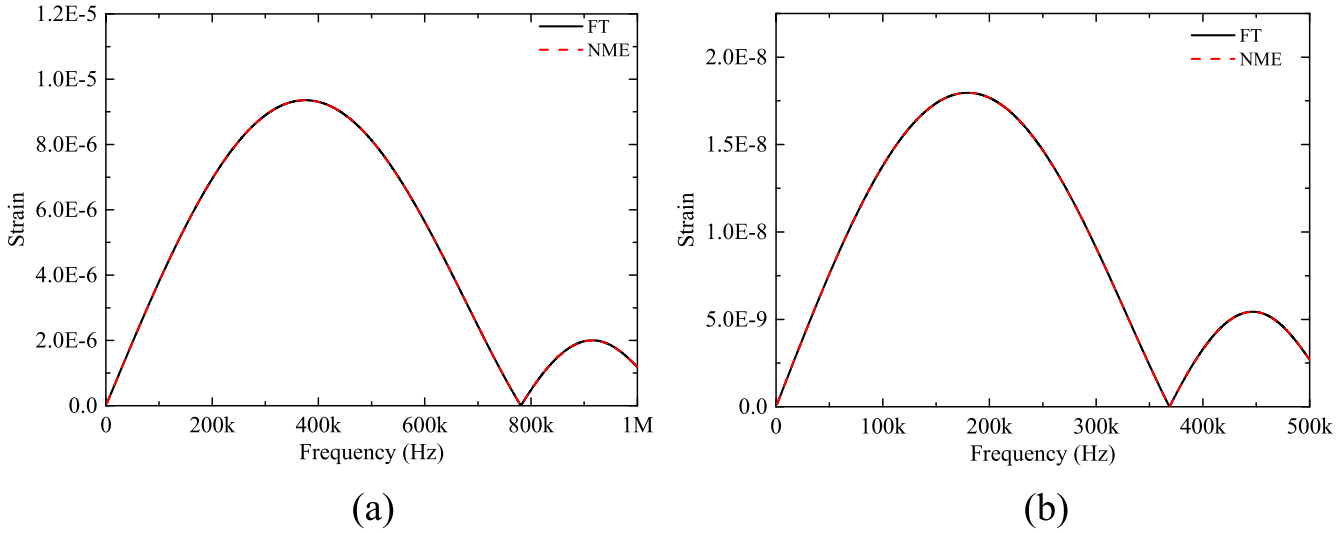

Figure 2. Frequency tuning curve comparison between the Fourier transform method and NME method in terms of strain responses: (a) linear S0 mode response; (b) AN-induced S0 mode response.

transform method, were well validated through both FE and experimental validations [22]. Here, the linear and AN-induced frequency tuning curves are calculated with the proposed NME method in order to validate its correctness through comparisons with the previous FT model.

In the validations, the width of the actuator is set to 8 mm as a representative case. Only the frequency tuning curves of the linear and AN-induced S0 mode Lamb waves are presented since the focus is on the SHM-promising primary S0-secondary S0 mode pair. The strain ε_{11} is used as the system output. For the linear and AN-induced responses, the sensing position is not important since neither the linear nor the AN-induced Lamb wave amplitude will vary with the propagating distance under the theoretical plane wave assumption. The results are shown in figure 2, which show a good consistency between the results obtained from the two methods.

FE validations of the frequency tuning of MNP-induced Lamb wave responses

To validate the MNP-induced responses, an FE model is built in ABAQUS with symmetric PZT bonding on the top and bottom surfaces of the plate to reduce the signal complexity. In this case, the S0 and A0 mode Lamb waves can be separately generated with either symmetrical or anti-symmetrical excitations. The nonlinear elastic properties of the materials are defined with the UMAT module. The maximum element size is set to 0.2 mm, which ensures more than 20 elements per smallest wavelength under consideration. Excitation signals with the same duration time are adopted for different frequencies.

To extract the second harmonic amplitude from the FE results, a superposition method, which superposes the responses from two inversed excitations, is first used to obtain the nonlinear signal components in the time-domain. Then complex morlet wavelet transform is applied to further extract their amplitude. Details of the signal processing method can be found in [22].

Before investigating the frequency tuning curves of the MNP-induced Lamb waves, a representative case with a 440 kHz excitation is presented. The second harmonic wave amplitude is first calculated with respect to the wave propagating distance with the proposed theoretical model, as shown in figure 3(a). It can be observed that the amplitude of the MNP-induced responses bounds with respect to the wave propagating distances at this specific frequency. Similar trend can be found from the time-domain signals received at different locations in the FE simulations (figure 3(b)). Taking the FE-calculated amplitudes of the five-time traces from figure 3(b) and putting them back to figure 3(a) show a nice agreement with the results calculated using the present model. This indicates that the MNP-induced frequency tuning curves will vary with the wave propagating distances, which is different from the AN-induced responses.

For further model validation, the wave propagation distances are set at 50 and 100 mm as two representative cases. The normalized frequency tuning curves obtained from both the proposed model and the FE simulations are shown and compared in figure 4. In both cases, the general tendency of the frequency tuning curves from both methods agrees well. In addition, the dependence of the MNP-induced frequency tuning characteristics on the wave propagating distances is evident, especially in terms of the peak and valley locations. To conclude, the effectiveness of the proposed method is confirmed by FE results.

System design to mitigate the AN

The validated theoretical model is further applied to design an NLW-SHM system through exploiting the dominance level of the MNP-induced and AN-induced responses. Prior to the system design process, it is worth noting that the shear-lag solutions are only valid in the low-frequency range since the dynamic characteristics of the actuators are not taken into account. This simplification was shown to be acceptable when the shear-lag parameter Γ is larger than $\sqrt{\omega^2\rho_a/E_a}$ [26]. This

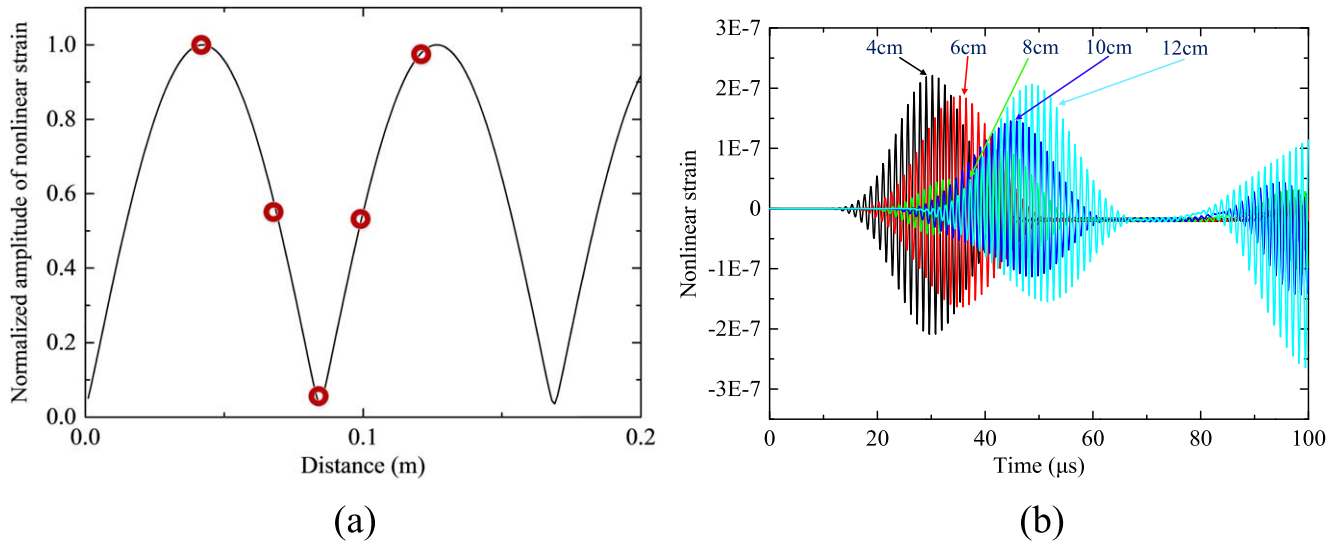

Figure 3. The MNP-induced Lamb wave responses at 440 kHz: (a) bounding amplitude of the nonlinear strains with propagating distances from the theoretical results; the five points marked in 'o' represent the amplitudes taken from FE simulations. (b) Nonlinear strains in time-domain at different propagating distances from FE results.

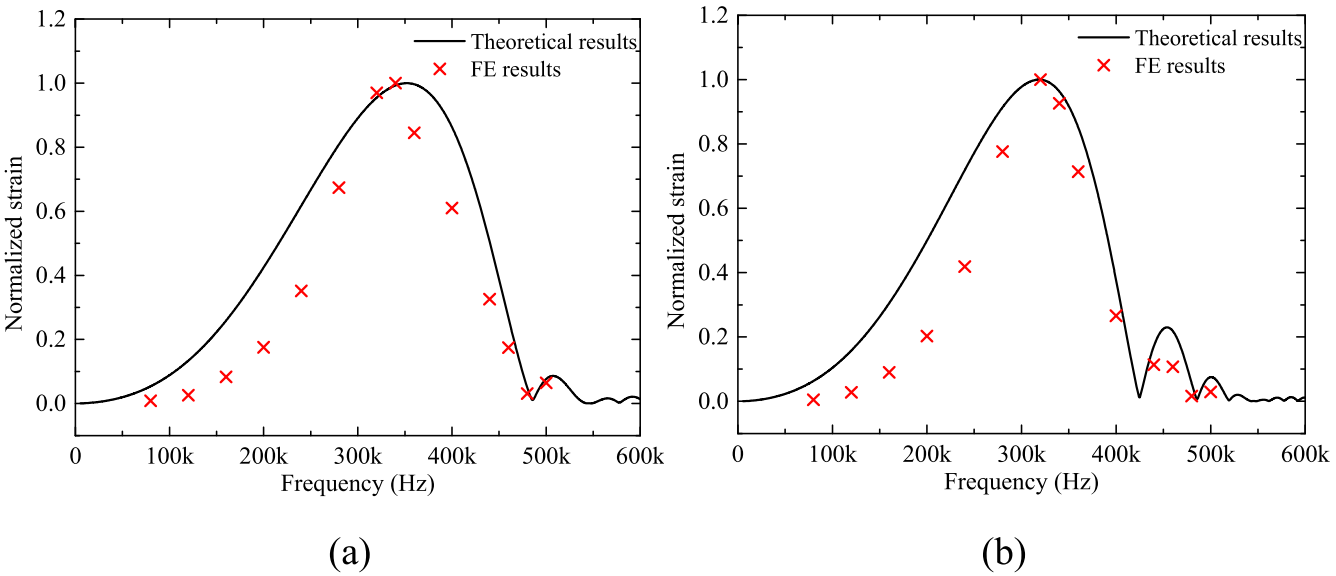

Figure 4. Comparison between the theoretical and FE-calculated frequency tuning curves of the MNP-induced Lamb waves for different wave propagating distances: (a) 50 mm; (b) 100 mm.

gives the corresponding upper limit of the model in terms of a frequency f_{up} which can be estimated by

$$f_{up} = \frac{1}{2\pi}\sqrt{\frac{E_a\Gamma^2}{\rho_a}}, \tag{14}$$

where ρ_a is the mass density of the PZT actuator. This limit also applies to the calculations on both linear and MNP-induced responses. However, for the AN-induced responses, as the AN-induced solutions are basically the extension of the classic shear-lag solution to the second order, the upper limit of frequency should be accordingly reduced to $f_{up}/2$. Consequently, the frequency range in the system design process should be capped below $f_{up}/2$.

The goal of the design is to mitigate the adverse effect of the AN through adjusting the various system parameters such as the width or the thickness of the PZT actuators, thickness of the bonding layers, or their material properties and so on. Among all these parameters, the width of the actuator is probably the easiest one to change in the practical perspective, which is also the most effective one according to the frequency tuning curves. Therefore, the width of the PZT is taken as the tuning parameter here to illustrate the process. Three typical PZT width cases are considered: 8, 18 and 40 mm. In each case, the frequency tuning curves of the second harmonic S0 mode Lamb waves induced by AN and MNP can be calculated with the proposed model to find the effective excitation frequency. Then, the corresponding FE models with the obtained actuator widths and the corresponding excitation frequencies are built to further validate the designed systems. The wave propagating distance is set to

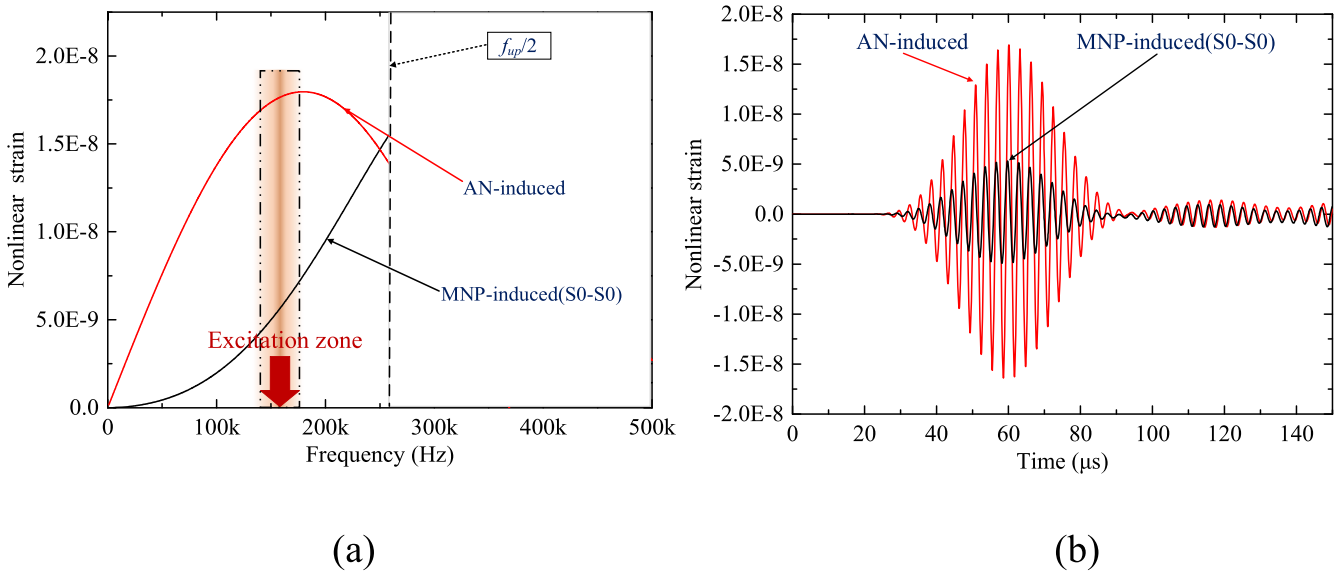

Figure 5. Evaluation results for the system with 8 mm wide PZT: (a) theoretical frequency tuning curves; (b) FE results of the second harmonic responses with 160 kHz excitations.

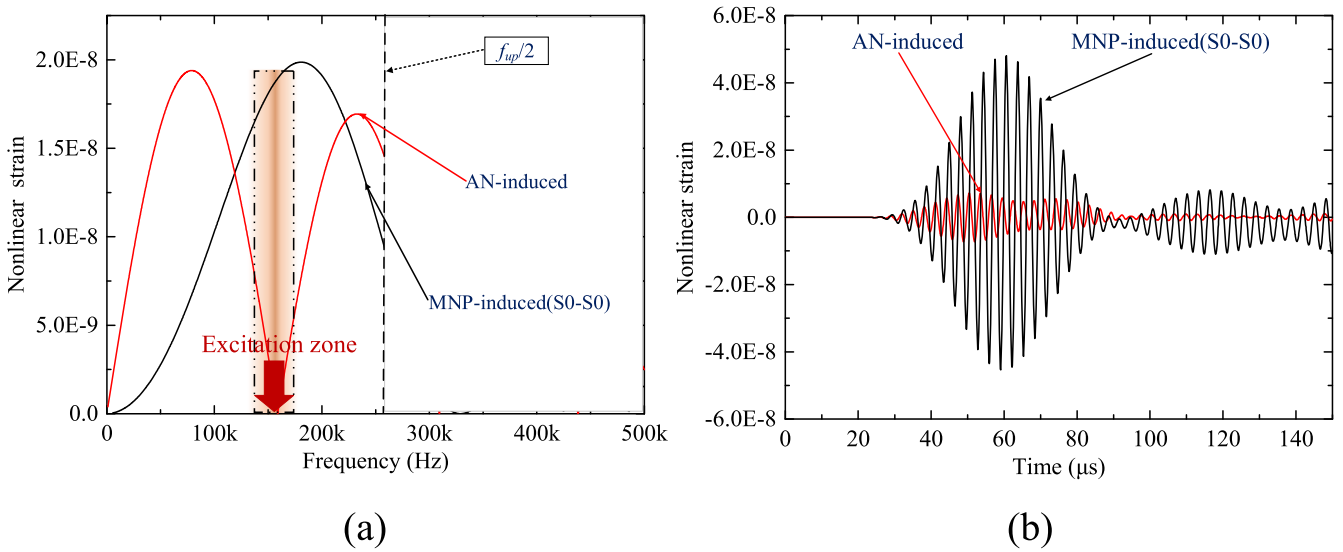

Figure 6. Evaluation results for the system with 18 mm wide PZT: (a) theoretical frequency tuning curves; (b) FE results of the second harmonic responses with 160 kHz excitations.

100 mm in all cases. Both theoretical and FE results are illustrated from figures 5 to 7 for the three different cases.

For the first case, based on the frequency tuning curves (figure 5(a)), the AN-induced second harmonic response is more significant than the MNP-induced one within the frequency range of interest. This means that, irrespective of the excitation frequency, the influence of the AN is always dominant in the system, overwhelming that of the MNP. As a simple validation case, we take the excitation frequency at 160 kHz and carry out the FE simulations in which the AN and MNP are separately introduced to the model. The corresponding nonlinear strains (shown in figure 5(b)) are extracted with the superposition method. It can be seen that the amplitude of the AN-induced second harmonic S0 Lamb waves is indeed larger than its counterpart induced by MNP, which agrees with the theoretical predictions. In the second case with the 18 mm wide PZT, theoretical results (figure 6(a)) show that in the specific frequency range around 160 kHz, the AN-induced response reaches the minimum around the valley of the frequency tuning curves, which is a preferred scenario for SHM applications. In this case, the wavelength of the AN-induced S0 mode Lamb waves is close to the PZT width. Similarly, the corresponding FE simulations are also carried out at 160 kHz, with the results shown in figure 6(b). Again, the FE results are consistent with the theoretical results, showing the mitigated and much reduced AN as compared with its MNP counterpart. Similarly, for the last case with the 40 mm wide PZT, theoretical results indicate that around 70 kHz, the AN can be mitigated in the system, as depicted in figure 7(a), again confirmed by the FE results in figure 7(b).

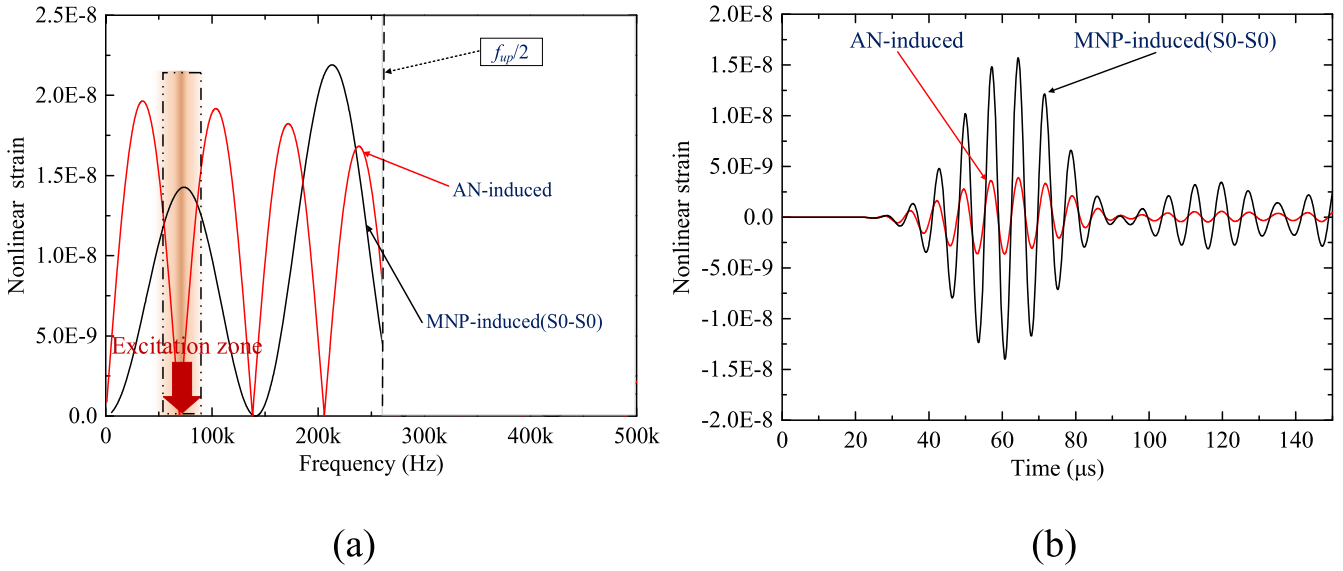

Figure 7. Evaluation results for the system with 40 mm wide PZT: (a) theoretical frequency tuning curves; (b) FE results of the second harmonic responses with 70 kHz excitations.

In the last two cases, the excitation frequency is selected near the valley of the frequency tuning curves of the AN-induced responses to minimize the influence of AN in the system. In these cases, the PZT widths are close to the corresponding wavelengths of the AN-induced Lamb waves. If defining the ratio between the amplitude of MNP-induced response and that of the AN-induced response (A_{MNP}/A_{AN}) as the mitigation efficiency, the mitigation efficiency of the third system is lower than that of the second system, as evidenced by the FE results in figures 6(b) and 7(b). This can be attributed to the influence of the excitation bandwidth on the frequency tuning characteristics. More specifically, in the FE simulations or the further experiments, the excitation signals are tone-burst signals, which inevitably have a certain bandwidth near the selected center frequency in the spectrum. The frequency components near the central frequency in the frequency tuning curves will also affect the final responses. With the increase of the PZT width, the gaps between the peaks in the frequency tuning curves become narrower. When the excitation frequency band is located near the valley of the AN-induced frequency tuning curve, the narrower gap leads to the larger amplitude of the AN-induced wave components at the frequencies near the valley, as sketched in figures 6(a) and 7(a). As a result, the mitigation efficiency is compromised in the last case.

To sum up, the width of the PZT should be carefully designed when developing NLW-SHM systems. Generally, the PZT width should be selected to match the wavelength of the AN-induced S0 mode Lamb waves. In real applications, if the PZT is very narrow, AN may not be effectively mitigated due to the frequency upper limit. In addition, a very wide PZT in the NLW-SHM system may compromise the mitigation efficiency of AN since the gaps between the peaks of the AN-induced frequency tuning curves are narrow.

Influence of A0–S0 mode pair on the system

In most practical applications, PZT actuators can be bonded only on one side of the plate. In this case, A0 mode Lamb waves will also be generated alongside the S0 waves in the low-frequency range. In principle, the A0 mode Lamb waves can also generate the second harmonic S0 mode Lamb waves since the power flux from the primary A0 mode Lamb waves to the secondary S0 mode Lamb waves is non-zero. However, due to the large differences between the phase velocities of the primary A0 and second harmonic S0 mode Lamb waves in the low-frequency range, the cumulative characteristic of this specific mode pair is significantly impaired so that such induced second harmonic S0 mode Lamb waves can be negligible in most cases.

To confirm this, the second system with the 18 mm wide PZT used in the previous section is revisited. The frequency tuning results are calculated using the presently proposed model, corresponding to the three different second harmonic generation mechanisms, as shown in figure 8(a). It can be seen that the A0 mode induced responses are non-negligible only at very low frequencies. Above roughly 50 kHz, the influence of the primary A0 mode Lamb waves can indeed be neglected, which should be the case for most NLW-SHM systems used in practice. Upon extracting the different second harmonic components at 160 kHz, FE simulations also demonstrate the same phenomenon as shown in figure 8(b).

Experimental investigations

Experiments are carried out to further validate the systems designed in the previous section. Specifically, two systems are highlighted: one as the 'optimized system' with a 18 mm wide actuator and the other one as an 'arbitrary system' with an 8 mm wide actuator.

Experimental strategy with thermal aging test

Consider the two sets of transducers bonded on an aluminum plate (2024-T3), of 600 mm × 500 mm × 2 mm in size, as

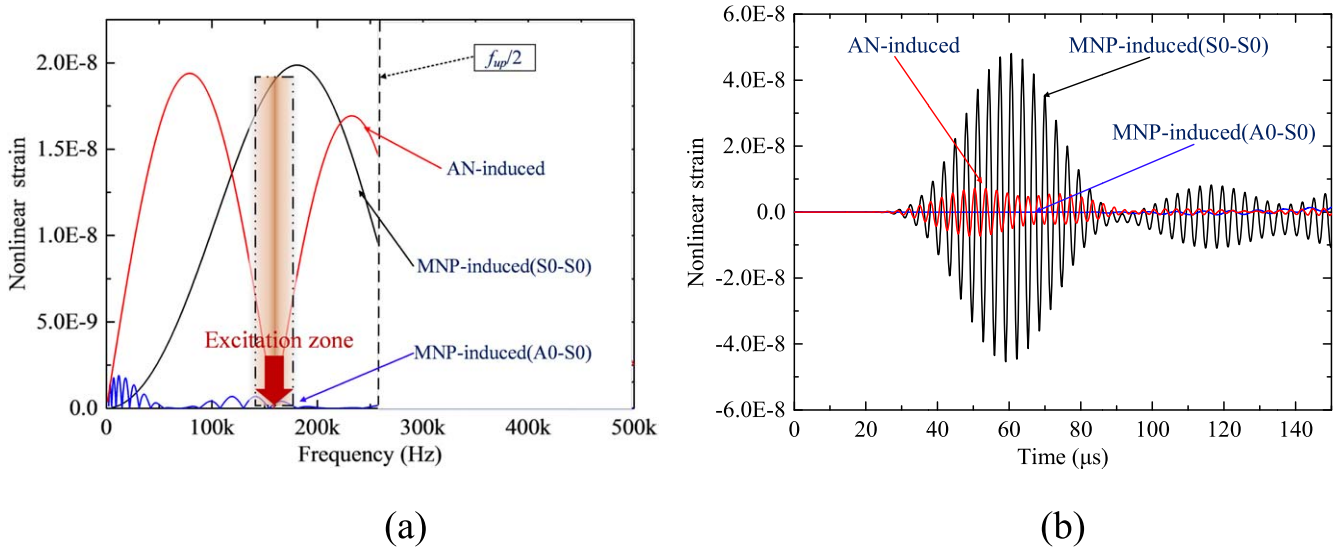

Figure 8. Influence of the primary A0 mode Lamb waves on the second harmonic generation for the system with 18 mm wide PZT: (a) theoretical predictions of the frequencies tuning curves; (b) FE results of the second harmonic responses with 160 kHz excitations.

shown in figure 9. Actuator A1 and A2 are, respectively, 18 mm and 8 mm in width corresponding to the two systems that were defined previously. The length and the thickness of both actuators are identical as 30 mm and 0.3 mm respectively. The dimensions of the sensors S1 and S2, 300 mm away from the actuators, are 5 mm × 5 mm × 0.3 mm. Thus, actuator A1 and sensor S1 correspond to the so-called optimized system while A2 and S2 are associated with the so-called arbitrary system. To keep the PZT edges as parallel as possible, we first drew parallel lines in the plate and then bonded the PZTs by making reference to these lines. This way, we believe the PZT installation error was minimized so that the influence of unparallelism is negligible. It is worth noting that in the previous section on system design, the wave propagation distance is set to 100 mm. However, as the AN-induced frequency tuning curves are independent of the wave propagating distances, the AN is still expected to be mitigated in the optimized system.

In order to evaluate the dominance level of the nonlinear sources in the systems, material nonlinear properties of the plate are tactically changed. If the MNP is dominant in the system, a change in the material nonlinear properties will induce significant changes in the captured nonlinear responses. Otherwise, the changes in the nonlinear responses will be hardly observed. Thermal aging is a well-known and effective process to change the microstructures and material nonlinear properties [25, 27]. The technique is adopted in the present experiment. Specifically, the center area (100 mm × 100 mm) of the plate was heated to around 350 °C for 4 h. To prevent the heat transfer from the heating area to the transducer-plate interfaces, which would cause changes in the material properties of the bonding layers or even jeopardize their normal operation to the extreme case, heat barriers were installed. These heat barriers, shown in figure 9, were realized with continuously flowing water to keep the bonding layers at the room temperature. It is worth noting that even at a lower heating temperature, the use of a heat barrier is still essential

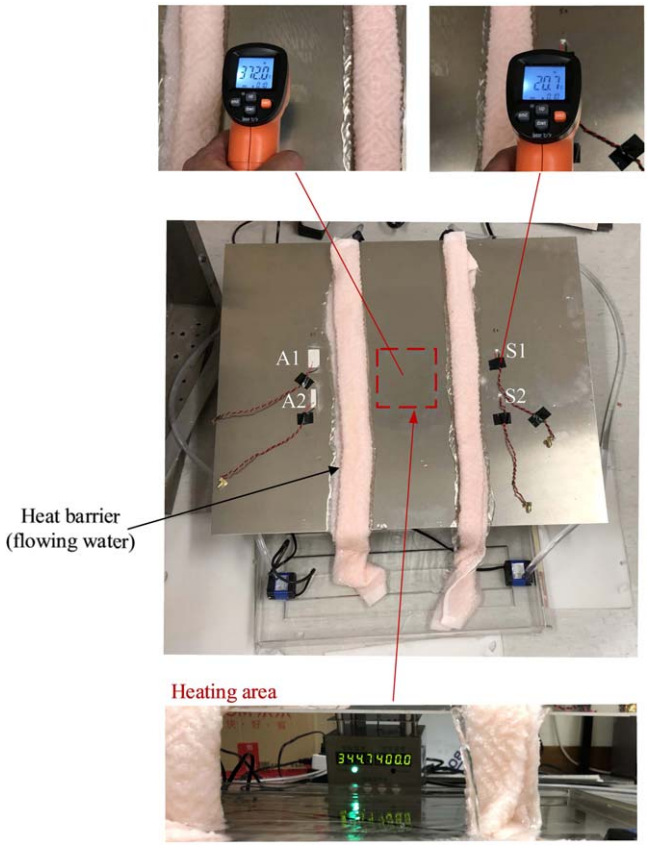

Figure 9. Experimental configuration and thermal aging treatment.

to prevent changes in the material properties of the bonding layers, especially their nonlinear behavior. Without the heat barriers, changes in the captured nonlinear responses would result from both AN and MNP. Consequently, their respective contributions cannot be separated and evaluated.

Tests were performed before and after the heating. The experimental set-up and procedure are identical to our previous

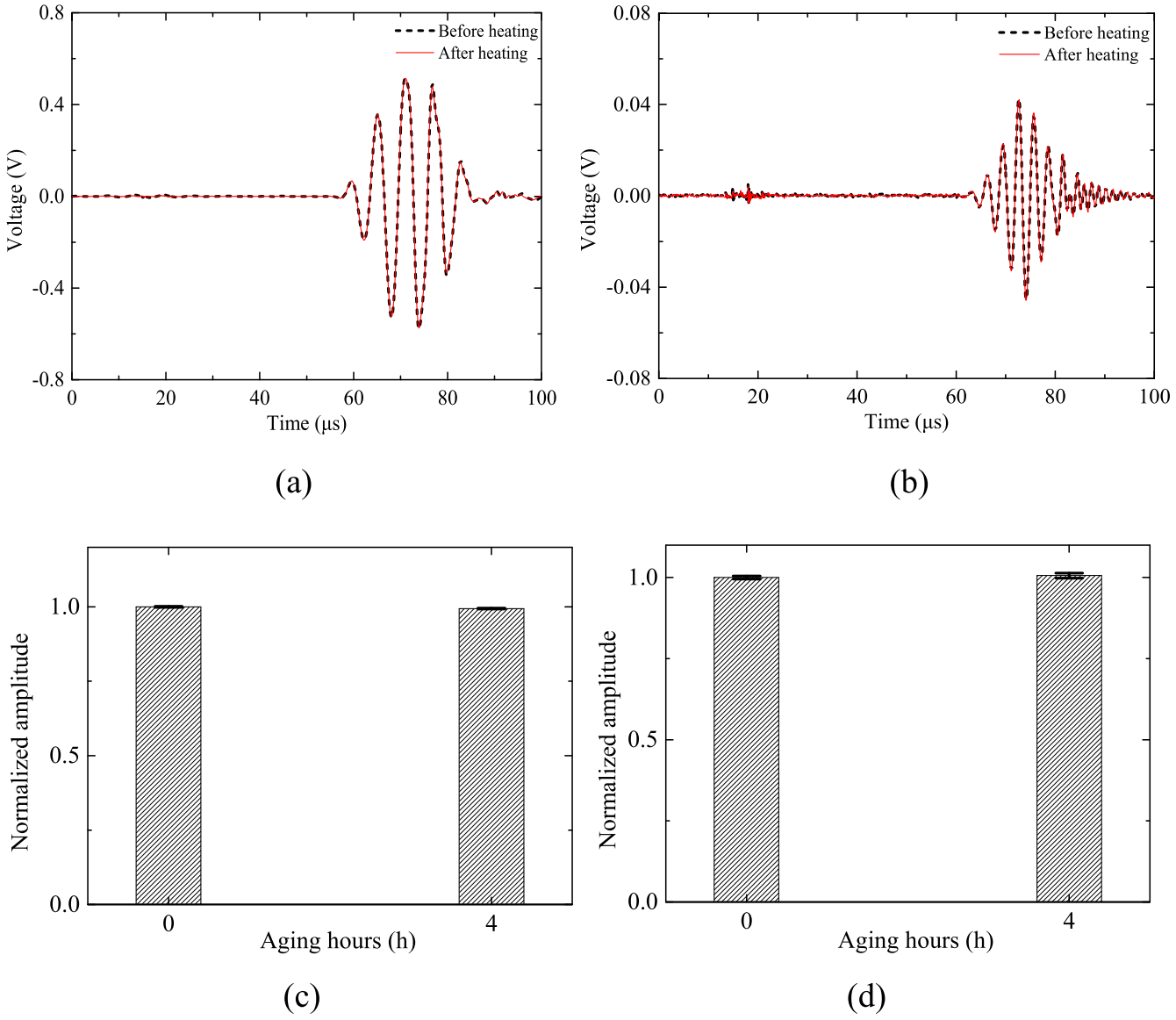

Figure 10. Experimental results for the arbitrary system before and after thermal aging: (a) linear time-domain responses; (b) second harmonic time-domain responses; (c) linear amplitude with error bars; (d) second harmonic amplitude with error bars.

work [22]. A pair of 5 cycle tone-burst excitation signals of 200 V at 160 kHz with inversed voltage was applied to the actuators. The same signal extraction method, which is detailed in the previous section, was used to extract the amplitude of the nonlinear components. Four sets of tests were conducted: before and after the thermal aging using the optimized system and the arbitrary system, respectively. For each test, 100 signals were recorded and averaged to reduce the measurement noise. In addition, the process was repeated four times to further calculate the variation range of the results.

Results and discussions

Results for the arbitrary system are first presented in figures 10(a) and (b), which correspond to the linear and nonlinear signals averaged with 100 signals before and after the heating. The signal to noise ratio is good even for the nonlinear responses. After extracting the amplitude of the signals for the four repetitive tests and normalizing to the intact case, the corresponding mean amplitudes (bars) with variation plots (lines on the top of the bars) are shown in figures 10(c) and (d). Results show very slight changes in both the linear (0.6% decrease) and nonlinear responses (0.59% increase) despite the heating which theoretically should change the MNP. This demonstrates the overwhelming effect and the dominance of the AN in a system which is not optimized. By the way, it is relevant to note that the variation among various tests is very small, which also demonstrates that the transducers and the corresponding bonding layers are well protected by the designed heat barrier.

Following the same procedure, test results for the optimized system are illustrated in figure 11. Results indicates a slight decrease (7.6%) in the linear responses, as shown in figures 11(a) and (c). By contrast, there is a dramatic increase (254%) in the nonlinear responses in figures 11(b) and (d). Since the

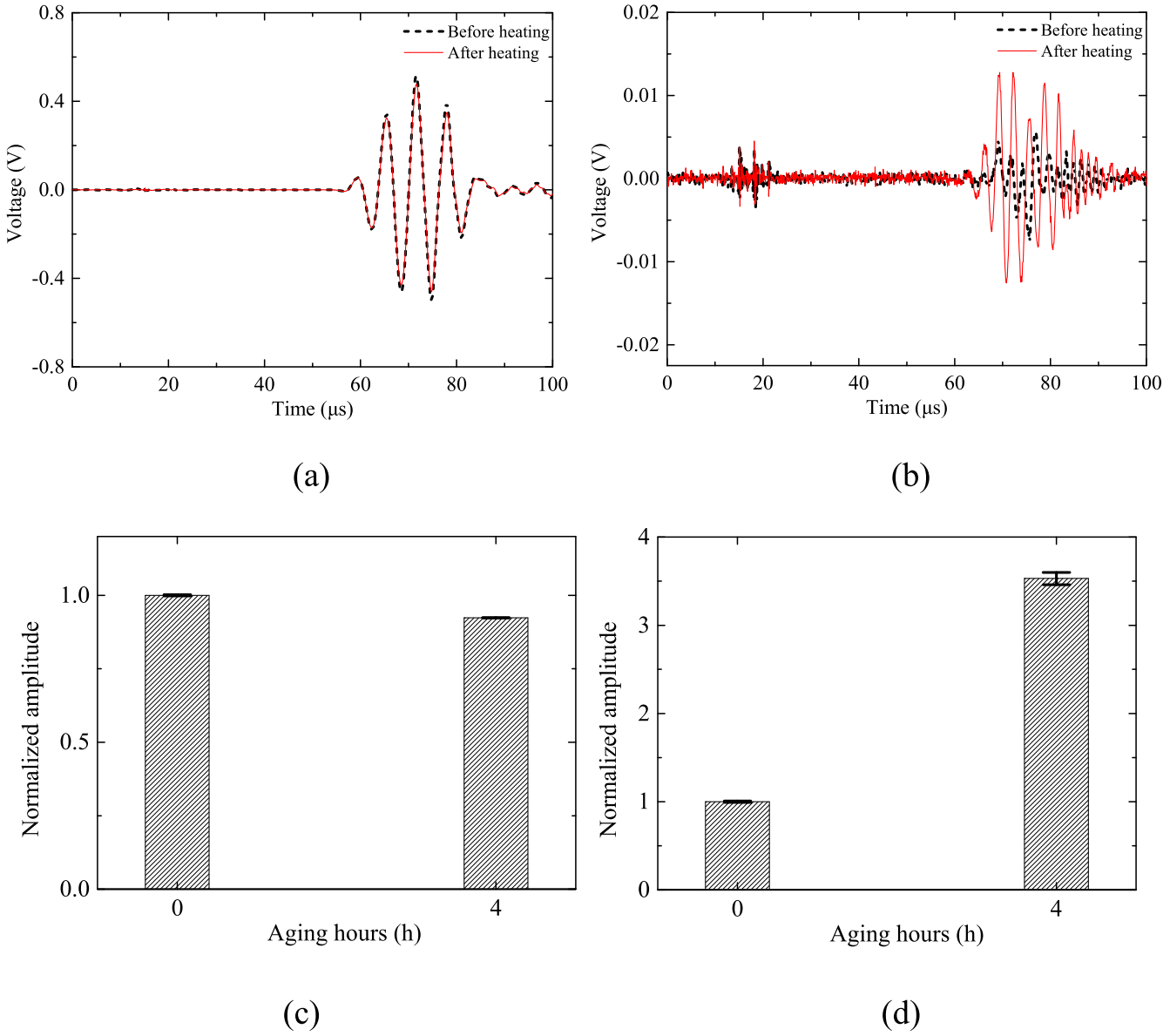

Figure 11. Experimental results for the effective system before and after thermal aging: (a) linear time-domain responses; (b) second harmonic time-domain responses; (c) linear amplitude with error bars; (d) second harmonic amplitude with error bars.

transducers are shown to be well protected by the heat barriers, this dramatic increase in the nonlinear responses in the system can only be attributed to the changes in the MNP as a result of the thermal aging treatment. In addition, comparing the changes in the linear (figure 11(c)) and nonlinear (figure 11(d)) responses in the optimized system, it can be concluded that the nonlinear Lamb waves are indeed much more sensitive to the micro-structural changes induced by the thermal aging process than linear Lamb waves are, as one might expect. Most importantly, the significant changes in the nonlinear responses in figure 11(d) confirm that the MNP becomes dominant in the system owing to the effective mitigation of the AN.

To sum up, experiments clearly establish the fact that AN can be effectively mitigated so that the MNP can be detected and monitored as an indicator of the structural damage. This can be achieved through a proper system design with the help of the proposed model, which is of great significance for guiding the design of NLW-SHM systems.

Conclusions

This paper proposes a comprehensive theoretical model by combining a nonlinear shear-lag model and the NME method to investigate both the AN and the MNP in a PZT-activated NLW-SHM system. The model allows embedding both the AN and MNP under the same roof, thus enabling direct comparisons between the two types of important nonlinearities in the system. Moreover, endowed with the capability of scrutinizing various nonlinear components and simulating the entire wave propagation process, the model is further used to design practical NLW-SHM systems to mitigate the undesired and adverse effect of the

AN. FE simulations are used to validate and confirm the proposed model as well as various physical phenomena. In particular, the frequency tuning curves of the MNP-induced Lamb waves and the effectiveness of the designed systems are verified by tactically adjusting different nonlinear sources. Finally, the designed optimized system is verified by experiments, in comparison with an arbitrarily chosen one. The dominant level of the nonlinear sources in the two systems is evaluated through a thermal aging treatment which effectively changes the MNP-related microstructures in the plate. Both FE simulations and experimental results demonstrate that AN can be effectively mitigated through proper system design so that the MNP can be detected and monitored as the indicator of the structural damage.

The proposed theoretical model enables insightful understandings on the PZT-driven NLW-SHM systems as it systematically includes both AN and MNP. Specifically, the frequency tuning characteristic of the AN-induced Lamb waves is independent on the wave propagating distances as opposed to that of the MNP-induced Lamb waves. In addition, the influence of the primary A0-secondary S0 mode pair due to the MNP is negligible in real SHM applications due to the severe phase velocity mismatching between the primary and secondary waves. The theoretical model also indicates AN can be mitigated if the PZT width is close to the wavelength of the AN-induced Lamb waves. Nevertheless, the PZT width should not be neither too small nor too large. For the former, the excitation frequency corresponding to the matched wavelength may exceed the frequency range of interest, whilst for the latter, the mitigation efficiency of the AN could be compromised since the gaps between the peaks of the AN-induced frequency tuning curves are narrow.

The understandings revealed by the current investigation can provide useful guidance to the design of an NLW-SHM system in terms of selection of the optimal system configurations, like the PZT width and excitation frequencies. With the design of an effective system, SHM actions will be further carried out to detect incipient damages in our future work.

Acknowledgments

This work was supported by a grant from the Innovation and Technology Commission of the HKSAR Government to the Hong Kong Branch of National Rail Transit Electrification and Automation Engineering Technology Research Center and the Research Grants Council of Hong Kong Special Administrative Region (PolyU 152070/16E).

Appendix. Lamb wave structures

For the nth symmetric or anti-symmetric mode Lamb waves, the velocities and stress across the thickness can be expressed as [24]:

$$\begin{aligned} v_{Sx}(y) &= i\omega B_n(\xi_{Sn}\cos(\alpha_{Sn}y) - R_{Sn}\beta_{Sn}\cos(\beta_{Sn}y)) \\ v_{Sy}(y) &= -\omega B_n(\alpha_{Sn}\sin(\alpha_{Sn}y) + R_{Sn}\xi_{Sn}\sin(\beta_{Sn}y)), \end{aligned} \quad (A.1)$$

$$\begin{aligned} v_{Ax}(y) &= i\omega A_n(\xi_{An}\sin(\alpha_{An}y) - R_{An}\beta_{An}\sin(\beta_{An}y)) \\ v_{Ay}(y) &= \omega A_n(\alpha_{An}\cos(\alpha_{An}y) + R_{An}\xi_{An}\cos(\beta_{An}y)), \end{aligned} \quad (A.2)$$

$$\begin{aligned} T_{Sxx}(y) &= -i\mu B_n[(\xi_{Sn}^2 + \beta_{Sn}^2 - 2\alpha_{Sn}^2)\cos(\alpha_{Sn}y) \\ &\quad - 2R_{Sn}\xi_{Sn}\beta_{Sn}\cos(\beta_{Sn}y)] \\ T_{Syy}(y) &= i\mu B_n[(\xi_{Sn}^2 - \beta_{Sn}^2)\cos(\alpha_{Sn}y) \\ &\quad - 2R_{Sn}\xi_{Sn}\beta_{Sn}\cos(\beta_{Sn}y)] \\ T_{Szz}(y) &= -i\lambda B_n(\xi_{Sn}^2 + {\alpha_{Sn}}^2)\cos(\alpha_{Sn}y) \\ T_{Sxy}(y) &= \mu B_n[2\xi_{Sn}\alpha_{Sn}\sin(\xi_{Sn}y) \\ &\quad + R_{Sn}(\xi_{Sn}^2 - \beta_{Sn}^2)\sin(\beta_{Sn}y)], \end{aligned} \quad (A.3)$$

$$\begin{aligned} T_{Axx}(y) &= -i\mu A_n[(\xi_{An}^2 + \beta_{An}^2 - 2\alpha_{An}^2)\sin(\alpha_{An}y) \\ &\quad - 2R_{An}\xi_{An}\beta_{An}\sin(\beta_{An}y)] \\ T_{Ayy}(y) &= \mu A_n[(\xi_{An}^2 - \beta_{An}^2)\sin(\alpha_{An}y) \\ &\quad -2R_{An}\xi_{An}\beta_{An}\sin(\beta_{An}y)] \\ T_{Azz}(y) &= -i\lambda A_n(\xi_{An}^2 + {\alpha_{An}}^2)\sin(\alpha_{An}y) \\ T_{Axy}(y) &= -\mu A_n[2\xi_{An}\alpha_{An}\cos(\xi_{An}y) \\ &\quad + R_{An}(\xi_{An}^2 - \beta_{An}^2)\cos(\beta_{An}y)], \end{aligned} \quad (A.4)$$

where

$$\alpha^2 = \frac{\omega^2}{c_p^2} - \xi^2, \quad \beta^2 = \frac{\omega^2}{c_s^2} - \xi^2, \quad (A.5)$$

$$R_S = \frac{(\xi_S^2 - \beta_S^2)\cos(\alpha_S d)}{2\xi_S\beta_S\cos(\beta_S d)}, \quad R_A = \frac{(\xi_A^2 - \beta_A^2)\sin(\alpha_A d)}{2\xi_A\beta_A\sin(\beta_A d)}. \quad (A.6)$$

In the equations, the subscripts S and A represent the symmetric and anti-symmetric Lamb wave modes, respectively. d is the half plate thickness. c_p and c_s are the longitudinal and shear wave speeds, respectively. ξ denotes the wave number for either symmetric or anti-symmetric modes according to its subscript.

ORCID iDs

Shengbo Shan https://orcid.org/0000-0002-0950-6193
Li Cheng https://orcid.org/0000-0001-6110-8099

References

[1] Farrar C R and Worden K 2007 An introduction to structural health monitoring *Phil. Trans. R. Soc.* A **365** 303–15
[2] Su Z, Ye L and Lu Y 2006 Guided Lamb waves for identification of damage in composite structures: a review *J. Sound Vib.* **295** 753–80
[3] Staszewski W J 2004 *Advances in Smart Technologies in Structural Engineering* (Berlin: Springer) pp 117–62
[4] Masserey B and Fromme P 2013 Fatigue crack growth monitoring using high-frequency guided waves *Struct. Health Monit.* **12** 484–93
[5] Zhao X, Gao H, Zhang G, Ayhan B, Yan F, Kwan C and Rose J L 2007 Active health monitoring of an aircraft wing with embedded piezoelectric sensor/actuator network: I. Defect detection, localization and growth monitoring *Smart Mater. Struct.* **16** 1208

[6] Shan S, Qiu J, Zhang C, Ji H and Cheng L 2016 Multi-damage localization on large complex structures through an extended delay-and-sum based method *Struct. Health Monit.* **15** 50–64
[7] Chillara V K and Lissenden C J 2015 Review of nonlinear ultrasonic guided wave nondestructive evaluation: theory, numerics, and experiments *Opt. Eng., Bellingham* **55** 011002
[8] Matlack K, Kim J-Y, Jacobs L and Qu J 2015 Review of second harmonic generation measurement techniques for material state determination in metals *J. Nondestruct. Eval.* **34** 273
[9] Xiang Y, Deng M, Xuan F-Z and Liu C-J 2011 Experimental study of thermal degradation in ferritic Cr–Ni alloy steel plates using nonlinear Lamb waves *Ndt & E Int.* **44** 768–74
[10] Deng M and Pei J 2007 Assessment of accumulated fatigue damage in solid plates using nonlinear Lamb wave approach *Appl. Phys. Lett.* **90** 121902
[11] Pruell C, Kim J-Y, Qu J and Jacobs L J 2007 Evaluation of plasticity driven material damage using Lamb waves *Appl. Phys. Lett.* **91** 231911
[12] Yan-Xun X, Fu-Zhen X and Ming-Xi D 2010 Evaluation of thermal degradation induced material damage using nonlinear Lamb waves *Chin. Phys. Lett.* **27** 016202
[13] Deng M 2003 Analysis of second-harmonic generation of Lamb modes using a modal analysis approach *J. Appl. Phys.* **94** 4152–9
[14] Srivastava A and di Scalea F L 2009 On the existence of antisymmetric or symmetric Lamb waves at nonlinear higher harmonics *J. Sound Vib.* **323** 932–43
[15] Liu Y, Chillara V K and Lissenden C J 2013 On selection of primary modes for generation of strong internally resonant second harmonics in plate *J. Sound Vib.* **332** 4517–28
[16] De Lima W and Hamilton M 2003 Finite-amplitude waves in isotropic elastic plates *J. Sound Vib.* **265** 819–39
[17] Bermes C, Kim J-Y, Qu J and Jacobs L J 2007 Experimental characterization of material nonlinearity using Lamb waves *Appl. Phys. Lett.* **90** 021901
[18] Wan X, Tse P, Xu G, Tao T and Zhang Q 2016 Analytical and numerical studies of approximate phase velocity matching based nonlinear S0 mode Lamb waves for the detection of evenly distributed microstructural changes *Smart Mater. Struct.* **25** 045023
[19] Wan X, Peter W T, Chen J, Xu G and Zhang Q 2018 Second harmonic reflection and transmission from primary S0 mode Lamb wave interacting with a localized microscale damage in a plate: a numerical perspective *Ultrasonics* **82** 57–71
[20] Sun X, Liu X, Liu Y, Hu N, Zhao Y, Ding X, Qin S, Zhang J, Zhang J and Liu F 2017 Simulations on monitoring and evaluation of plasticity-driven material damage based on second harmonic of S0 mode Lamb waves in metallic plates *Materials* **10** 827
[21] Hong M, Su Z, Wang Q, Cheng L and Qing X 2014 Modeling nonlinearities of ultrasonic waves for fatigue damage characterization: theory, simulation, and experimental validation *Ultrasonics* **54** 770–8
[22] Shan S, Cheng L and Li P 2016 Adhesive nonlinearity in Lamb-wave-based structural health monitoring systems *Smart Mater. Struct.* **26** 025019
[23] Shan S, Cheng L and Wen F 2018 Characterization of nonplanar second harmonic Lamb waves with a refined nonlinear parameter *J. Nondestruct. Eval., Diagn. Prognostics Eng. Syst.* **1** 011004
[24] Kamal A and Giurgiutiu V 2014 Shear horizontal wave excitation and reception with shear horizontal piezoelectric wafer active sensor (SH-PWAS) *Smart Mater. Struct.* **23** 085019
[25] Hasanian M and Lissenden C J 2017 Second order harmonic guided wave mutual interactions in plate: vector analysis, numerical simulation, and experimental results *J. Appl. Phys.* **122** 084901
[26] Dugnani R 2016 Extension of the Crawley's adhesive model to dynamically actuated piezoelectric transducers *J. Intell. Mater. Syst. Struct.* **27** 2112–24
[27] Alexopoulos N D 2009 On the corrosion-induced mechanical degradation for different artificial aging conditions of 2024 aluminum alloy *Mater. Sci. Eng.* A **520** 40–8